Available online at www.sciencedirect.com
ScienceDirect
Trans. Nonferrous Met. Soc. China 35(2025) 2612−2631
Transactions of Nonferrous Metals Society of China
www.tnmsc.cn

Microstructure, electrochemical, wear and corrosive wear performance of laser-based powder bed fusion and wrought biomedical Ti−6Al−4V alloys

A. G. LEKATOU[1,2], B. V. EFREMENKO[3], V. HAOUI[1], V. G. EFREMENKO[3,4], S. EMMANOUILIDOU[1], V. I. ZURNADZHY[3,4], I. PETRYSHYNETS[4], Yu. G. CHABAK[3,4], I. I. SILI[3]

1. Laboratory of Applied Metallurgy, Department of Materials Science and Engineering, School of Engineering, University of Ioannina, Ioannina 45110, Greece;
2. Institute of Materials Science and Computing, University Research Center of Ioannina (URCI), Ioannina 45110, Greece;
3. Department of Physics, Pryazovskyi State Technical University, Dnipro 49044, Ukraine;
4. Institute of Materials Research of Slovak Academy of Sciences, Kosice 04001, Slovakia

Received 1 January 2024; accepted 27 August 2024

Abstract: Wrought and laser powder bed fusion (LPBF) Ti−6Al−4V (Ti-6-4) specimens were comparatively evaluated, with the objective to determine LPBF Ti−6Al−4V's suitability for biomedical applications. Testing included nanoindentation, cyclic polarization in simulated body fluid (SBF, 37 °C), and dry and SBF "ball-on-plate" sliding. Wrought Ti-6-4 exhibited a lamellar $\alpha+\beta$ microstructure, whereas LPBF Ti-6-4 displayed a fine-grained α'-martensite microstructure. LPBF Ti-6-4 demonstrated ~3% higher indentation modulus and ~32% higher hardness, while wrought Ti-6-4 showed ~8% higher plasticity. Both alloys exhibited low corrosion rates (10^{-5} mA/cm^2 order) and true passivity (10^{-4} mA/cm^2 order). No localized corrosion was observed in either two alloys, except for occasional metastable pitting in the LPBF alloy. However, LPBF Ti-6-4 presented higher corrosion rate and passive current, ascribed to its martensitic structure. During dry sliding, LPBF Ti-6-4 exhibited ~14% lower volume loss compared to wrought Ti-6-4. Sliding in SBF increased volume losses for both alloys, with wear resistances nearly equalized, as the advantage of LPBF Ti-6-4 decreased due to more intense wear-accelerated corrosion induced by the stressed martensite. Overall, the results demonstrate the suitability of LPBF Ti-6-4 for biomedical uses.

Key words: biomedical Ti−6Al−4V alloy; laser-based powder bed fusion; electrochemical corrosion; nanoindentation; sliding wear; wear-corrosion synergism

1 Introduction

The simultaneous possession of corrosion resistance, wear resistance and mechanical strength is crucial for surgical implants, impacting antibacterial properties, functionality and durability. For non-biodegradable metallic biomaterials, the higher the corrosion resistance, the better the biocompatibility [1]. Ti−6Al−4V (Ti-6-4) is the most common alpha−beta Ti-alloy for biomedical applications, offering low weight, good corrosion resistance, strength, and biocompatibility [2,3]. However, it has low wear resistance under sliding or fretting conditions and high surface friction coefficient, which can be problematic in joint implants [4−6]. This may lead to toxic effects due to accumulation of wear debris and release of vanadium and aluminum ions [6].

Additive manufacturing (AM) is increasingly

Corresponding author: V. G. EFREMENKO, E-mail: vgefremenko@gmail.com
https://doi.org/10.1016/S1003-6326(25)66836-1

popular for producing high-quality metallic components at lower costs and shorter lead times [7]. AM involves melting or consolidating feedstock using an energy source in an incremental, layered manner, creating a three-dimensional component directly from a computer model without molds or tooling [8]. Selective laser melting (SLM) or laser-based powder bed fusion (LPBF) is an efficient AM method for small batches of complex metallic parts, using a laser to melt metal powder layer by layer [9].

As Ti-6-4 is the most commercialized titanium alloy nowadays, there is a growing interest in manufacturing it by AM methods, like LPBF, DED (directed energy deposition), EBM (electron beam melting), LMD (laser metal wire/powder deposition), SMD (shaped metal deposition) and WAAM (wire arc additive manufacturing) [10−14], and studying their effect on the microstructure and crucial properties such as corrosion and wear resistance. However, rapid cooling, multiple thermal cycles and high temperature gradients (as in LPBF) may induce residual stresses, high-density defects, porosity and the formation of brittle martensitic (α') structures [15−19], with possible adverse effects on the corrosion and wear performance.

Recent studies have explored the corrosion performance of LPBF Ti-6-4. QIN et al [20] found that high compression strains reduced corrosion resistance in 3.5 wt.% NaCl solution due to the deformed α' phase. In an earlier study, QIN et al [21] noted that increasing NaCl concentration in the solution enhanced both corrosion resistance and surface film thickness. CHEN et al [22] observed slightly inferior corrosion behavior in dynamic Hank's solution compared to static conditions, primarily attributed to mass-transfer effects. BOWER et al [23] reported the development of a mixed TiO_2 and Al_2O_3 layer on LPBF Ti-6-4 that was stabilized after ~400 h of salt spraying. WANG et al [24] highlighted that heat treatment improved the corrosion resistance of LPBF Ti−5Cu, by promoting Ti_2Cu formation that slowed the microgalvanic reaction between Ti_2Cu and α'/α-Ti and enhanced the stability of the passive film. DAI et al [25] associated the anisotropy in the corrosion resistance of different planes of LPBF Ti-6-4 in 1 mol/L HCl with different amounts of α' and β phases in their microstructures.

However, the findings on the corrosion evaluation of the LPBF Ti-6-4 compared to traditionally prepared analogues are often contradictory. Some studies reported poorer corrosion resistance for LPBF Ti-6-4 in NaCl, NaOH, H_2SO_4 and simulated body fluid (SBF) solutions, attributed to the predominance of high-energy metastable martensite [26−29]. Unlike forged Ti-6-4, DMLS (direct metal laser sintered) Ti-6-4 was found susceptible to crevice corrosion in physiological medium, because of its high grain boundary area [30]. Conversely, CECCHEL et al [31] noted a slightly better corrosion resistance for LPBF Ti-6-4 in 3.5 wt.% NaCl solution compared to wrought Ti-6-4. JU et al [32] also reported better corrosion resistance in artificial saliva compared to wrought and heat-treated Ti-6-4, attributed to hydrophobicity, high grain boundary density and uniform alloying element distribution. VILHENA et al [33] attributed the slightly higher corrosion resistance of LPBF Ti-6-4 in artificial saliva, compared to powder metallurgy fabricated Ti-6-4, to its fine microstructure. The fine and uniform $\alpha'+\beta$ microstructure, which enhanced passivation ability, was considered responsible for the greater corrosion resistance of LPBF Ti-6-4 compared to its cast counterpart in hot nitric acid containing oxidizing ions [34].

Works comparing the wear and tribocorrosion behavior between LPBF and conventional Ti-6-4 are also contradictory. CECCHEL et al [31] found similar dry sliding wear resistance for LPBF and forged Ti-6-4, with a slight superiority of the latter. Similar wear rates and other dry sliding characteristics were exhibited by LPBF, EBM and conventional Ti-6-4 [35]. Contrarily, BARTOLOMEU et al [36] reported higher sliding wear resistance for LPBF Ti-6-4 in phosphate buffered saline (PBS) fluid compared to cast, and hot-pressed Ti-6-4, due to martensite presence. ZHU et al [37] reported that the decreasing sliding wear rate under lubrication for differently prepared Ti-6-4 alloys followed the sequence: wrought > LPBF > heat-treated LPBF, with the heat-treated alloy having the lowest wear rate due to the formation of a tribo-oxide layer. ZHANG et al [38] and HUANG et al [26] reported greater dry sliding wear resistance for LPBF and EBM Ti-6-4 over forged variants, attributing it to martensite predominance. In contrast, KANG et al [39] noted the lowest wear rates for wrought Ti-6-4 compared

to LPBF and LDED (laser-directed energy deposition) Ti-6-4, which associated the inferior wear performance of LPBF Ti-6-4 with its brittleness.

The tribocorrosion performance of LPBF Ti-6-4 for biomedical applications has received less attention than its corrosion and wear performance. HUANG et al [26] found that the tribocorrosion resistance in 0.9 wt.% NaCl was significantly affected by the corrosion conditions, with forged Ti-6-4 outperforming LPBF Ti-6-4. Contrariwise, TOPTAN et al [40] noticed similar volume losses for LPBF and hot-pressed Ti-6-4 in 9 g/L NaCl solution, despite the inferior corrosion behavior of LPBF. VILHENA et al [33] reported similar wear rates for LPBF and conventional Ti-6-4 in artificial saliva. CHIU et al [41] observed that both LPBF and conventional Ti-6-4 exhibited similar corrosion rates under tribocorrosion testing in SBF, despite LPBF's superior wear resistance, due to the formation of n-type semiconductor surface layers that adsorbed chlorine.

Within the above framework, and given the often contradictory studies on the corrosion, wear and tribcorrosion behaviors of AM and conventional Ti-6-4 for biomedical applications, this work adopts a holistic approach. It evaluates the microstructure, electrochemical, and tribological responses of wrought and LPBF Ti-6-4 in SBF at 37 °C.

2 Experimental

Plates of Ti-6-4 with dimensions of 5 mm × 10 mm × 20 mm were fabricated by LPBF using a 3D printer (ProX DMP 320 by 3D Systems), as previously detailed in Refs. [7,42]. The powder feedstock (average particle size of (39±3) μm) was supplied by "Electro-Optical Systems". Its nominal chemical composition (wt.%) was: 5.5−6.75 Al, 3.5−4.5 V, O < 0.2, N < 0.05, C < 0.08, H < 0.015, Fe < 0.3, and Ti balanced. LPBF Ti-6-4 was compared with commercial wrought Ti-6-4 (hereafter denoted as "WR") supplied as an 8 mm-thick plate with a chemical composition (wt.%) of 5.90 Al, 4.24 V, 0.01 Si, 0.02 Fe, 0.005 C, and Ti balanced. WR Ti-6-4 had an ultimate tensile strength of 995 MPa and a total elongation of 14% (according to the delivery certificate).

The microstructure of the alloys was studied on specimens prepared by standard metallography procedures through grinding with SiC papers and polishing with Al_2O_3 aqueous suspensions. The polished specimens were etched by Kroll's reagent (5 mL HF, 5 mL HNO_3, and 90 mL H_2O). Microstructure observations were performed by optical microscopy (OM) using the Olympus GX71 microscope and scanning electron microscopy (SEM) using the JEOL 5600 and JEOL JSM−7000F microscopes. The SEM examination was carried out employing the secondary electron imaging (SEI) and backscattered electron composition (BEC) modes. The phase chemical composition was determined using an EDS detector (INCAx-sight by Oxford Instruments). The phase identification was carried out by X-ray diffraction/XRD (X'Pert PRO by PANalytical, Cu K_α). The grain size was determined by image analysis on 10 separate fields of 650 μm × 865 μm area, using the Image-Pro software. The quantitative phase composition of the alloys was also estimated by image analysis on 12 different fields of polished and etched surfaces, using the Image J software.

Electrochemical corrosion testing was carried out using polished specimens mounted in phenolic resin and peripherally covered by an insulating silane tape, leaving a surface area of ~1 cm^2 to be exposed to a simulated body fluid solution (SBF) with the following composition in 1 L of bidistilled water: 7.996 g NaCl, 0.350 g $NaHCO_3$, 0.224 g KCl, 0.228 g $K_2HPO_4·3H_2O$, 0.305 g $MgCl_2·6H_2O$, 40 mL 1 mol/L HCl, 0.278 g $CaCl_2$, 0.071 g Na_2SO_4, 6.057 g $NH_2C(CH_2OH)_3$, and a pH of 7.4 at 37 °C [43]. Potentiodynamic polarization tests were carried out connecting a standard three-electrode cell (reference electrode: Ag/AgCl/3.5 mol/L KCl; counter electrode: Pt gauze; working electrode: Ti-6-4 specimen) to the Gill AC (ACM Instruments) potentiostat/ galvanostat. After 1 h of holding under open circuit, potentiodynamic polarization started at a scan rate of 10 mV/min. The corrosion current densities were calculated using Tafel extrapolation; the extrapolation was applied to the cathodic portion of the polarization curves though linear regression of the potential versus the logarithm of current density data. To maintain accuracy, the calculations adhered to several constraints, detailed in previous efforts [44,45]. Corrosion rates were calculated from the corrosion current density values according to ASTM G102 [46]. The alloys' resistance to

localized corrosion was assessed using cyclic (or reverse) polarization. The fundamental idea behind this technique is that if, during the reverse anodic scan, the current density exceeds that of the forward anodic scan at the same potential, the localized corrosion will take place on the exposed surface; the increased "reverse" current density is owing to a more aggressive environment in the propagating pits or crevices. In such instances, a "negative" (i.e. clockwise) hysteresis loop is formed on the voltammogram [47,48]. The critical corrosion values were determined as the means of the results from five replicate experiments.

The micro-mechanical properties of the alloys were determined by the G200 Nano Indenter (Agilent Technologies) equipped with a Berkovich pyramid. Indentation test was performed with a displacement speed of 10 nm/s to reach a maximum penetration depth of 2 μm. Hundreds of indents were made by 10 × 10 grid with a distance of 50 μm between the imprints. The sliding wear behavior of the alloys was assessed according to the "ball-on-plate" scheme employing the Micron-tribo (Micron-System) tribometer. A counter Al_2O_3 ball of 3.0 mm in diameter accomplished 1500 reciprocating movements (each one 3.5 mm long) with a sliding speed of 7.0 mm/s under a normal load of 5 N. Sliding was performed at room temperature in both dry state and wet state (SBF solution). The sliding wear properties were evaluated by means of the coefficient of friction (COF) and volume loss (ΔV) determined as described in Refs. [42,49]. The tests were repeated 4−5 times and an average of the results was adopted as the ΔV value.

3 Results

3.1 Microstructure characteristics

Figure 1 presents the X-ray diffractograms of WR and LPBF Ti-6-4. Both XRD patterns are absolutely dominated by the presence of α-Ti (hcp-Ti). Four main differences are discerned between the two diffractograms. The peak at 2θ=38.6° is primary in the pattern of WR Ti-6-4, whereas the peak at 2θ=40.3° is primary in the pattern of LPBF Ti-6-4. Normally, the peak at 2θ=38.6° is primary in the pattern of β-Ti (PDF No. 44-1288), whereas the peak at 2θ=40.3° is primary

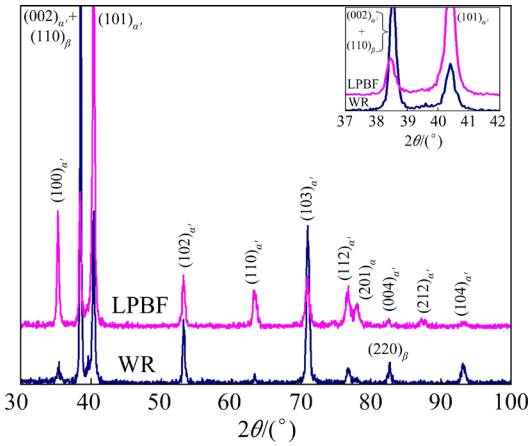

Fig. 1 XRD patterns of WR and LPBF Ti-6-4

in the pattern of α-Ti (PDF No. 44-1294). Furthermore, the peak at 2θ=35.3° with considerable intensity in the pattern of LPBF Ti-6-4 is minor in the pattern of WR Ti-6-4. This particular peak is significant in the pattern of α-Ti but absent from the pattern of β-Ti. In addition, the peak at 2θ=82.6°, which can be assigned to β-Ti (220), has a relatively high intensity in the pattern of WR Ti-6-4 but an insignificant intensity in the pattern of LPBF Ti-6-4 that probably corresponds to the $(004)_\alpha$ orientation. The above observations support the hypothesis that WR Ti-6-4 contains some β-phase as well, whereas LPBF Ti-6-4 consists almost entirely of α-phase. The fact that the peak at 2θ=38.6° is primary in the pattern of WR Ti-6-4 may as-well indicate a preferential orientation of the WR alloy. The fourth difference between the two diffractograms lies in the relatively broad diffraction peaks of LPBF Ti-6-4 as indicated by the values of the full width at half maximum (FWHM). The FWHM values are: 0.25° (WR) and 0.30° (LPBF) for the peak at 2θ=38.6°; 0.30° (WR) and 0.35° (LPBF) for the peak at 2θ=40.3°. This suggests the predominance of a distorted α-phase in the LPBF alloy, namely α'-Ti or hcp-martensite, commonly found in LPBF Ti-alloys, as reported in Section 1. Unfortunately, it is difficult to distinguish α and α' phases by XRD, as they crystallize in the same lattice (hcp) and have similar lattice parameters [50]. The martensitic transformation also generates remarkable residual stresses in the LPBF Ti-6-4 alloy [16]. So, the microstresses, lattice defects and supersaturation with V element, induced by sharp cycles of steep heating and cooling during the LPBF process have resulted in crystal deformation and XRD peak

broadening [19,28,42]. The suppression of the $\beta \rightarrow \alpha$ transformation due to rapid solidification (cooling rates involved 10^3−10^8 K/s [19]) probably caused the entrapment of V (β-Ti stabilizer) in the α-Ti lattice; the supersaturated α-lattice was deformed under the stresses of the V atoms and thermal stresses and was athermally transformed to martensite, a metastable phase in a highly-strained state. The findings of XRD are further elucidated by optical and SEM−EDS examination.

Figure 2 illustrates the microstructures of the WR Ti-6-4 specimens. Figure 2(a) shows that the

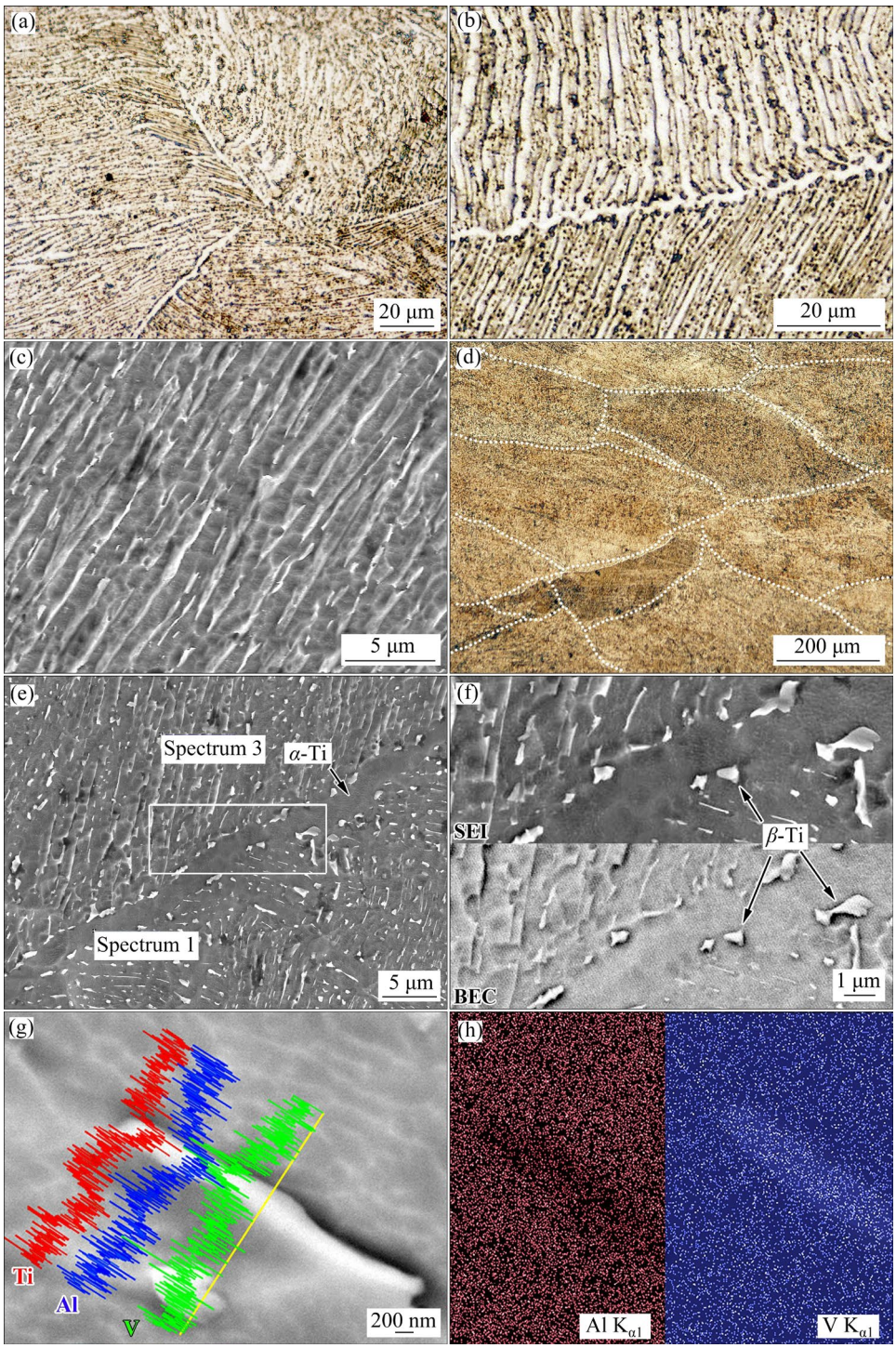

Fig. 2 (a−c) Microstructures of WR Ti-6-4 specimens revealing lamellar α+β; (d) Boundaries of prior β grains (denoted by dotted lines along with primary α network); (e) Microstructure detail around prior α boundary; (f) Different BEC-contrasts of β-phase and α-matrix within white-outlined rectangle in (e); (g) EDS line-scanning of Ti, Al and V across β-rod; (h) Al and V mappings of β-rod shown in (g); (a, b, d) OM; (c, e) SEM−SEI; (f) SEM−SEI−BEC; (g) SEM−BEC

microstructure of the WR Ti-6-4 consists of very fine lamellae of α and β phases, suggesting that forging-β and annealing-β (i.e. above β-transus) have taken place [3]. The boundaries are delineated by primary α that has formed at the grain boundaries of the initial grain β, during the rapid transition from the intermediate α+β phase regime to the α-phase stability regime (cooling from above β-transus to the ambient temperature). More analytically, when the temperature dropped below the β-transus temperature, the high temperature β-phase transformed to primary α, nucleating heterogeneously on the prior β columnar grains. The formation of primary α at the grain boundaries ended as soon as the temperature dropped below the α-transus temperature. Then, the remaining prior (high temperature) β phase transformed to lamellar α-Ti plates that started nucleating at the grain boundaries and grew along directions normal to them, thus consuming the pre-existing high-temperature β-phase [51]. The α-lamellae grew along selected crystallographic planes of pre-existing (prior) β phase, as seen in Figs. 2(a−c). The primary α network allowed to identify the boundaries of the prior β grains and estimate their shape and size range. As seen in Fig. 2(d), the WR alloy had a coarse-grained structure with a pronounced inequigranularity, mainly consisting of deformed coarse grains. The coarse grains had a length of up to 680 μm and a width of up to 250 μm. A minority of smaller grains, with lengths of 50−100 μm and widths of 40−70 μm, were also observed. The average longitudinal and transverse grain sizes were counted as (381±74) μm and (138±23) μm, respectively.

Phase identification was carried out by SEM−EDS in BEC mode on the basis of the following principle: as Al is an α-phase stabilizer, it is expected that the network of primary α along the grain boundaries will contain more Al and less V compared to the α+β structure inside the grains. This assumption was confirmed by point EDS measurements that revealed (5.7±0.1) wt.% Al and (2.3±0.2) wt.% V in the primary α network, whilst (5.4±0.4) wt.% Al and (5.3±0.6) wt.% V in the α+β areas (Spectra 1 and 3, respectively, in Fig. 2(e)). Hence, the very fine β-rods of preferential orientations that appeared dispersed within the α-matrix, presented lighter BEC-contrast than the α-phase due to their enrichment with a heavy element (vanadium, relative atomic mass Z_V=23) (Fig. 2(f)). The above postulation is confirmed by EDS line-scanning across a β-rod (Fig. 2(g)), which showed an uneven distribution of V, Al and Ti, with V content rising and Al and Ti contents dropping when crossing the β-rod. Similarly, EDS mapping of Al and V (Fig. 2(h)) of the β-rod, shown in Fig. 2(g), manifest the decreased concentration of Al and the increased concentration of V in the β-rod relative to the α-matrix. The volume fraction of β-phase in the wrought specimens was determined by image analysis as (20.68±4.73)%.

Figure 3 presents the microstructures of the LPBF Ti-6-4 specimens. The most distinguished feature is a “fish-scale” morphology resulting from layer-by-layer material consolidation during the LPBF process [7,42] (Fig. 3(a)). The hemispherical shape (Figs. 3(a, b)) reflects the shape of a liquid pool on the substrate surface melted under the laser beam (shown by arrows in Fig. 3(a)). The dark contrast (under an optical microscope) “boundary” of the hemisphere is associated with a melt pool contour. In SEM−SE mode, the “boundary” (shown in Fig. 3(b) by white dotted lines) has a slightly lighter contrast relative to the background of the martensitic structure, although in SEM−BEC mode, it is hardly distinguished from martensite. This indicates a uniform distribution of chemical elements in the analyzed area, which is confirmed by the linear distributions of Ti, Al, and V in Fig. 3(b) (note the absence of any significant fluctuations in the content of elements when crossing the “boundary”). As seen in Fig. 3(c), the “boundary” has a fine-cellular (<1 μm) structure “frozen” by rapid solidification in contact with an unmelted substrate [32]. Figure 3(d) reveals a martensitic microstructure with the needles of α'-martensite along different crystallographic planes formed due to the aforementioned high temperature gradients during the LPBF process, in compatibility with many works [15,19,25,28,52]. LPBF Ti-6-4 contained only minor amounts of β-phase ((1.35±0.31) vol.%), as determined by image analysis. Thus, the microstructure examination corroborates the XRD findings concerning the α/α'-status of LPBF Ti-6-4.

The boundaries of prior β-grains are delineated in Fig. 3(e). The grain size was calculated as (13.7±9.5) μm, which is more than one order of magnitude lower than that of the WR alloy. The fine-

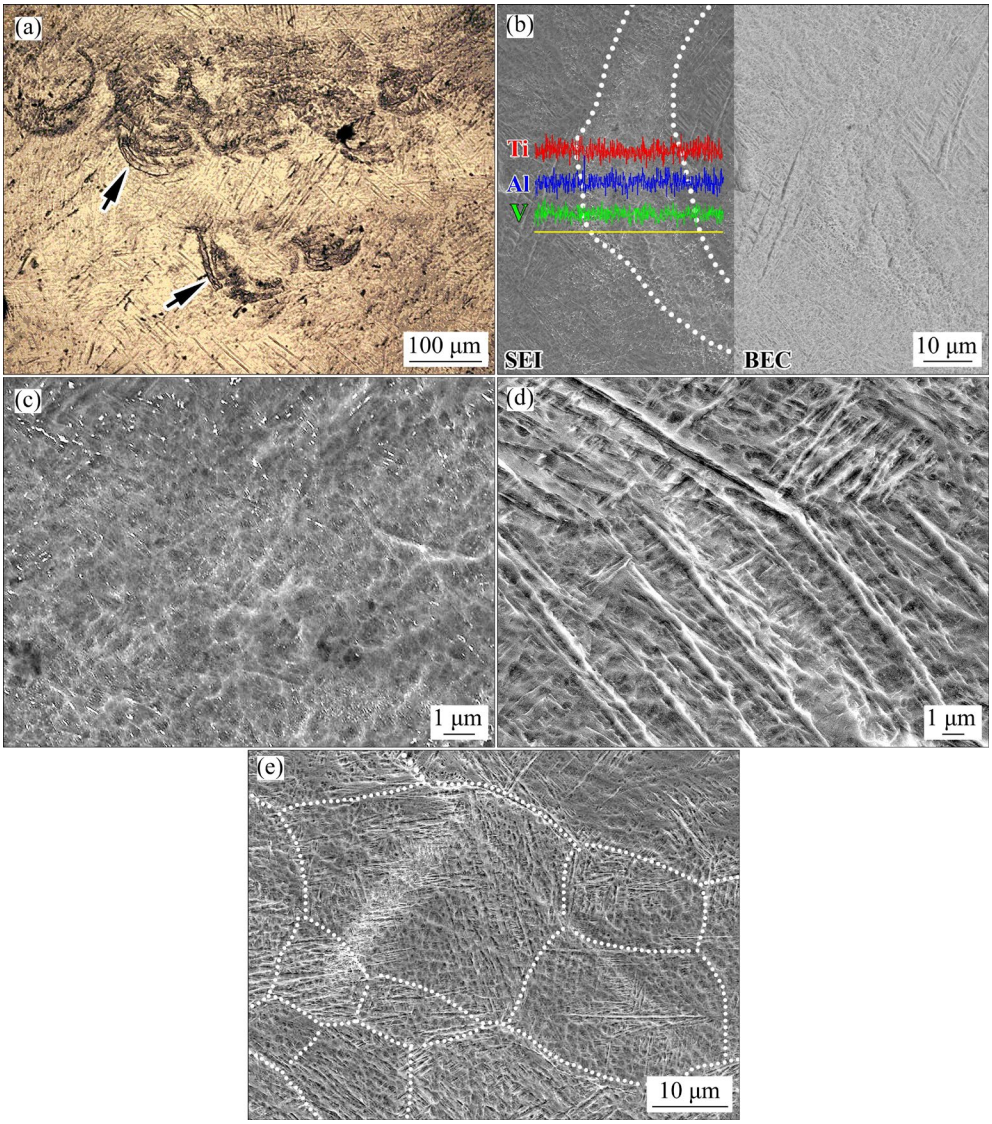

Fig. 3 Microstructures of LPBF Ti-6-4 specimens: (a) Fish-scale morphology; (b) EDS line-scanning across melt pool; (c) Fine cellular structure at boundary of melt pool; (d) Martensitic structure; (e) Boundaries of prior-β grains; (a) OM; (b) SEM−SEI−BEC; (c−e) SEM−SEI

grained status of the LPBF alloy is attributed to the high cooling rate under crystallization. The critical radius of the β-phase nucleus (r_β^*) can be given as [53]

$$r_\beta^* = \frac{2\sigma_{L/\beta}}{\Delta G_{L/\beta}} \quad (1)$$

where $\sigma_{L/\beta}$ is the energy of the "liquid/β nucleus" interface, and $\Delta G_{L/\beta}$ is the chemical driving force for β-nucleus solidification which depends on the supercooling degree (ΔT):

$$\Delta G_{L/\beta}=\Delta H_{L/\beta}-\Delta T\cdot S \quad (2)$$

where $\Delta H_{L/\beta}$ is the enthalpy change under crystallization, S is the entropy of the system, and $\Delta T=T_o-T_\beta$ (where T_o is the temperature of the liquid/β-phase equilibrium, and T_β is the temperature of the β-nucleus solidification).

From Eqs. (1) and (2), it follows that the critical radius of the β-phase is inversely proportional to ΔT. Taking into consideration the high cooling rates involved in the LPBF process (10^3−10^8 K/s [19]), it is presumed that the lagging of crystallization leads to the formation of β-phase at a temperature much lower than the equilibrium one, i.e. at a high ΔT. This leads to a remarkable decrease in r_β^* followed by the formation of fine β-grains. As such, the grains do not grow at a temperature above β-transus due to the suppression of the diffusion processes by rapid cooling. Hence,

the grains undergo the $\beta \rightarrow \alpha$ transformation at ~575 °C (M_s point of Ti-6-4 alloy [54]) being in a fine-sized state; thus, a fine-grained martensite structure can benefit the LPBF alloy's strength properties.

The described structural patterns of the LPBF alloy are attributed to the rigorousness of the 3D-printing process that induces numerous and interactive physical phenomena leading to topological, thermal and compositional gradients in the vicinity of the pool surface. The molten pools can be subjected to complex flow patterns owing to the simultaneous action of various factors, such as buoyancy forces resulting from temperature-dependent density differences within the pool and a transient Marangoni driven flow (thermocapillary convection) caused by a local superheat [55]. It is worth noting that the characteristic hierarchical cellular/columnar structure (associated with heat transfer under the LPBF process), which is a distinctive feature of 3D-printed alloys [7], has not been revealed in the structure of LPBF Ti-6-4. It is postulated that the cellular pattern was hidden by the martensitic needles which grew inside the prior β grains crossing the cellular sub-grains. Moreover, since the martensite formation is accompanied by shear deformation, this could affect the columnar texture by disordering the columnar (epitaxial) grain pattern.

3.2 Nanoindentation testing results

The micromechanical properties of WR and LPBF Ti-6-4 were determined by nanoindentation testing. The results of statistical data processing are shown in Table 1. As seen, the LPBF alloy exhibits higher average values for the following properties: indentation modulus by 3.5 GPa (2.8%) and indentation hardness by 1.06 GPa (32%). Moreover, the LPBF specimens show lower standard deviations (and less scatter): about 67% lower for the indentation modulus and approximately 40% lower for the indentation hardness.

Figure 4(a) displays the representative load−displacement curves for the LPBF and WR alloys, which correspond to the average values of the indentation hardness. It is seen that the load to indent to the targeted depth (2 μm) for LPBF Ti-6-4 is 75 mN higher than that of WR Ti-6-4, which indicates a higher strength for the LPBF alloy.

Table 1 Results of statistical processing of nanoindentation tests of Ti-6-4 specimens

Parameter	Indentation modulus/GPa		Indentation hardness/GPa	
	LPBF	WR	LPBF	WR
Range of values	124.2−136.7	113.7−135.7	4.14−4.86	2.84−3.80
Maximum data scatter	12.5	23.1	0.72	0.97
Mean value	129.6	126.1	4.42	3.36
Sigma (standard deviation)	2.67	4.80	0.17	0.24
Confidence interval	0.5	0.9	0.03	0.05

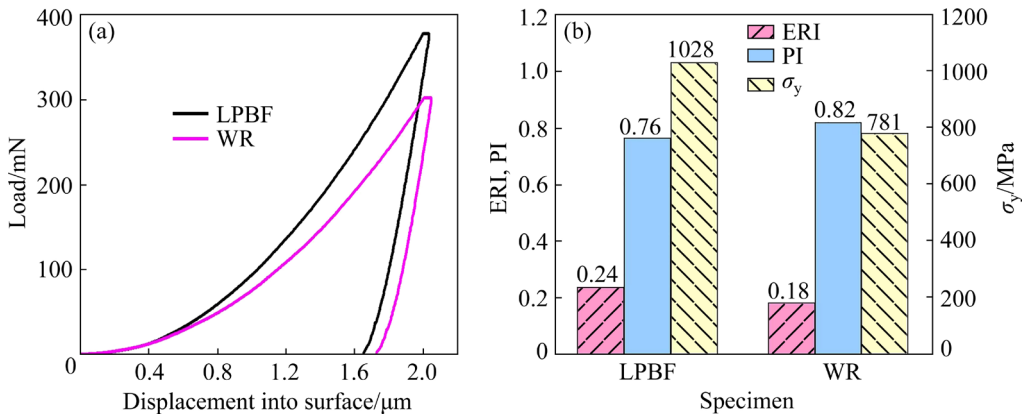

Fig. 4 Micromechanical properties of WR and LPBF Ti-6-4: (a) Characteristic load−displacement curves; (b) Values of ERI (elastic recovery index), PI (plasticity index) and σ_y (yield strength) derived from curves presented in (a)

The load−displacement curves allowed to derive some other parameters, which characterize the mechanical bahaviour of the material. One of them is yield strength (σ_y), which was calculated according to the Tabor equation [56]:

$$H=c\sigma_y \quad (3)$$

where H is the indentation hardness, and c is a fitting coefficient. According to the findings of RODRIGUEZ and GUTIERREZ [57], coefficient c has a constant value (4.3) for different alloys (steels, brass, and aluminium) if the nanoindentation depth is ≥2 μm, which is the present case.

Two additional parameters were derived from the load−displacement curves, which are associated with the work done by the indenter during the nanoindentation. These are the elastic recovery index (ERI) and the plasticity index (PI) [58]:

$$\mathrm{ERI}=W_e/W_t \quad (4)$$

$$\mathrm{PI}=W_p/W_t \quad (5)$$

where W_e and W_p are the elastic energy and plastic energy, respectively, defined by the area under the load−displacement curves according to ISO 14577-1; W_t is the total energy of nanoindentation ($W_t=W_e+W_p$).

The values of σ_y, ERI and PI calculated for the curves in Fig. 4(a), are presented in Fig. 4(b). The yield strength of the WR alloy was calculated as 781 MPa, which correlates with the results of the bulk tensile testing of the wrought plate (see Section 2). The σ_y value of the LPBF alloy was calculated as 1028 MPa, i.e. higher than that of the WR alloy by 237 MPa.

As follows from Fig. 4(b), the ERI, which reflects the energy dissipated from the specimens after load removal, is higher for the LPBF alloy, indicating the greater ability of the alloy to resist permanent deformation, as compared to the WR alloy. In turn, the WR alloy exhibits a higher PI, implying that the alloy underwent higher plastic deformation and manifested greater ductility under the nanoindentation testing. The greater ability of WR Ti-6-4 for plastic deformation is also qualitatively indicated by the (slightly) greater residual displacement, namely the final depth of the contact impression, in Fig. 4(a) [59].

3.3 Electrochemical corrosion testing results

Figure 5(a) compares the potentiodynamic polarization curves of the WR and LPBF specimens

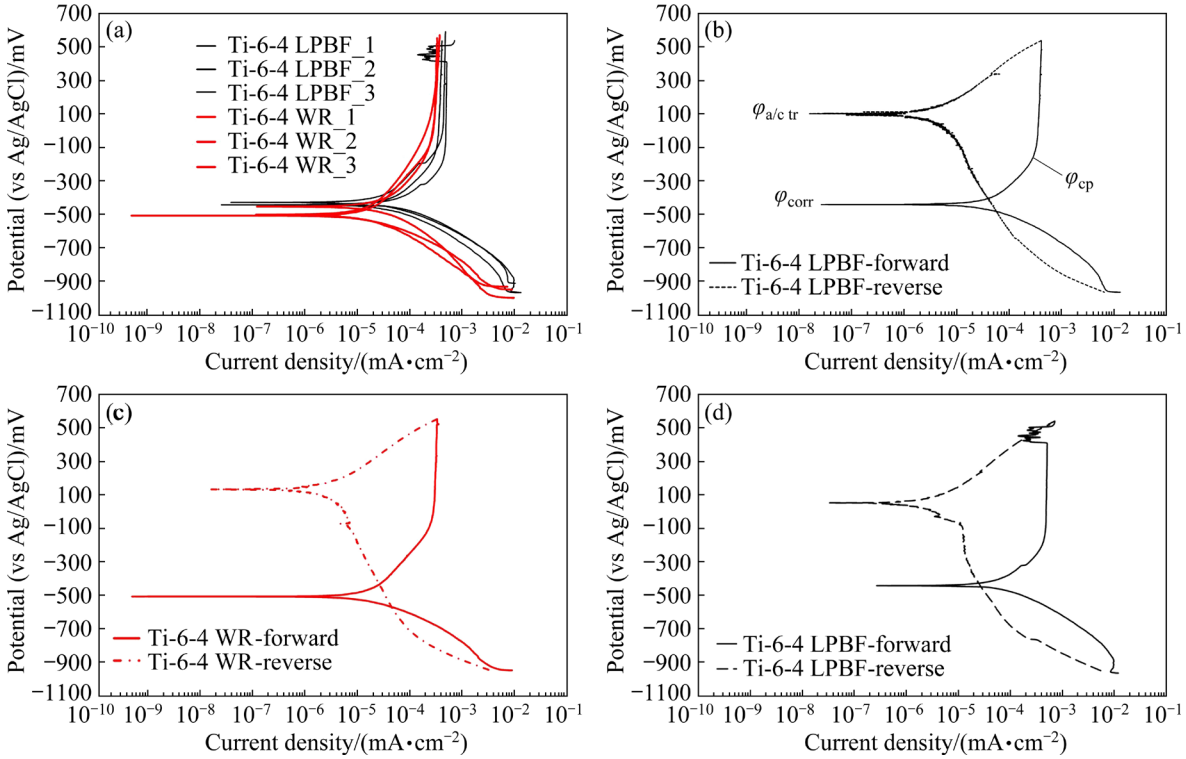

Fig. 5 (a) Voltammograms of LPBF and WR Ti−6−4; (b, c) Cyclic polarization curves of LPBF and WR Ti-6-4, respectively; (d) Cyclic polarization curves of LPBF Ti-6-4, presenting metastable pitting

during immersion in SBF at 37 °C. Both groups feature almost identical polarization curves with similar electrochemical values, the latter given in Table 2. The very low values of corrosion current density (J_{corr}) (order of 10^{-5} mA/cm^2) and the derived very low corrosion rates (order of 10^{-4} mm/a, 1 a=1 year) manifest the high resistance of both WR and LPBF alloys to general corrosion. In both cases, true passivity has been attained (passive current densities of the order of 10^{-4} mA/cm^2). Actually, in the range of potentials tested, passivity breakdown has not occurred.

The positive (counterclockwise) hysteresis loops in Figs. 5(b−d), the large surface areas of the positive hysteresis loops, the much higher $\varphi_{a/c\ tr}$ values compared to φ_{corr}, and the cross-sectional micrographs in Figs. 6(a, b) demonstrate that none of the alloys has undergone localized corrosion. Here, it is important to note that when $\varphi_{a/c\ tr}$ is nobler than φ_{corr}, it signifies a high resistance to localized corrosion for the following reasons [45]: A nobler $\varphi_{a/c\ tr}$ value in comparison with the φ_{corr} value means that the corroded surface starts to act as a cathode, and its dissolution is hindered by the non-corroded surface. Consequently, the non-corroded region corrodes preferentially, resulting in a uniform corrosion process that advances laterally across the surface. Conversely, when $\varphi_{a/c\ tr}$ is lower than φ_{corr}, the corroded surface will continue to function as an anode. This leads to increased corrosion of the corroded surface by the non-corroded surface, ultimately providing cathodic protection to the non-corroded area. As a result, the corrosion of the alloy primarily progresses in depth, resulting in the formation of numerous deep pits.

Figures 6(a, b) present the cross-sections of

Table 2 Electrochemical values of LPBF and WR Ti-6-4 immersed in SBF at 37 °C

Alloy	φ_{ocp}(vs Ag/AgCl)/ mV	φ_{corr}(vs Ag/AgCl)/ mV	φ_{cp}(vs Ag/AgCl)/ mV	$\varphi_{a/c\ tr}$(vs Ag/AgCl)/ mV	J_{corr}/ (mA·cm^{-2})	J_p/ (mA·cm^{-2})	R_{corr}/ (mm·a^{-1})	Pitting
LPBF	–412±34	–468±41	–184±18	130±66	(5.3±2.2)×10^{-5}	(4.5±0.4)×10^{-4}	(4.5±1.8)×10^{-4}	No (5/5)
WR	–407±39	–489±23	–92±14	109±24	(2.0±0.8)×10^{-5}	(3.0±0.3)×10^{-4}	(1.7±0.7)×10^{-4}	No (5/5)

φ_{ocp}: Open circuit potential; φ_{corr}: Corrosion potential; φ_{cp}: Critical passivation potential; $\varphi_{a/c\ tr}$: Anodic-to-cathodic transition potential; J_{corr}: Corrosion current density; J_p: Passive current density; R_{corr}: Corrosion rate; 5/5: Five out of five replicates showed no evidence of stable pitting

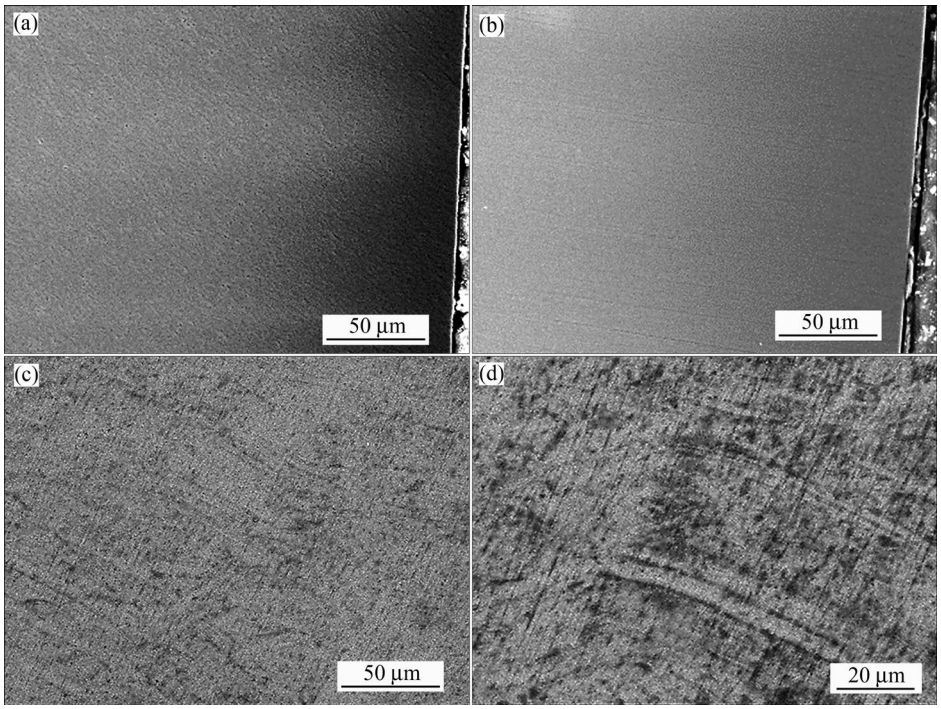

Fig. 6 Microstructures of alloys after cyclic polarization in SBF at 37 °C: (a, b) SEM−SEI cross-sections of LPBF and WR Ti-6-4, respectively; (c, d) SEM−SEI surface of LPBF Ti-6-4 at lower and higher magnifications, respectively

LPBF and WR Ti−6−4 specimens, respectively, after the cyclic polarization. A relatively low magnification was selected for a more objective view. A cross-sectional illustration was selected in order to assess the depth of corrosion. It is evident that corrosion has not progressed to any significant depth. Figures 6(c, d) illustrate the surface state of an LPBF specimen after cyclic polarization at a relatively low magnification (for a more objective view) and a higher magnification (for a more detailed view). The low magnification micrograph presents a surface with insignificant signs of corrosion (Fig. 6(c)), whereas the high magnification micrograph manifests that the surface has retained all its microstructural details (Fig. 6(d)). Figure 6(d) also reveals the sites that are potential corrosion-cell inducers like fish-scale boundaries with sub-micron porosity. The presence of sub-micron porosity can be attributed to thermal stresses.

Table 2 shows that LPBF Ti-6-4 presents higher corrosion rates and higher passivity current densities compared to WR Ti-6-4. It should also be noted that one out of five specimens of LPBF Ti-6-4 presented metastable pitting, in the form of anodic current transient spikes shown in Fig. 5(a) and more clearly in Fig. 5(d). Nevertheless, the metastable pits did not grow to stable pits during reverse polarization, as manifested by the counter-clockwise hysteresis loop of large surface area in Fig. 5(d). The metastable pitting behavior of LPBF Ti-6-4 is compatible with the higher passive current densities of LPBF Ti-6-4 as compared to WR Ti-6-4, as seen in Table 2. The properties and behavior mentioned above are attributed to the martensitic structure of the LPBF alloy.

3.4 Sliding wear testing results

The results of the sliding wear testing in dry and wet states are illustrated in Figs. 7 and 8. The comparison of the COF variations during sliding in Fig. 7 shows the similarity of the friction process for both alloys in both testing environments: the COF values widely fluctuate from less than 0.2 to 0.8, which characterizes the high intensity of the interaction of the sliding counter-bodies. Under dry sliding, the COF average values are 0.50 and 0.45 for WR and LPBF Ti-6-4, respectively (which is close to the COF value reported in Ref. [60] for the Ti-6-4/Al_2O_3 sliding couple). Table 3 shows that the LPBF alloy has lower values of 2σ interval (which covers 95% of the COF data points) and a lower mean COF as compared with the WR alloy. Comparison of Figs. 7(a) and (b) reveals a small decrease in the COF values for both alloys under wet sliding attributed to the lubricating action of the SBF solution. Overall, it is deduced that LPBF Ti-6-4 demonstrated a better antifriction capability than WR T-6-4 (actually, slightly better in the case of SBF sliding).

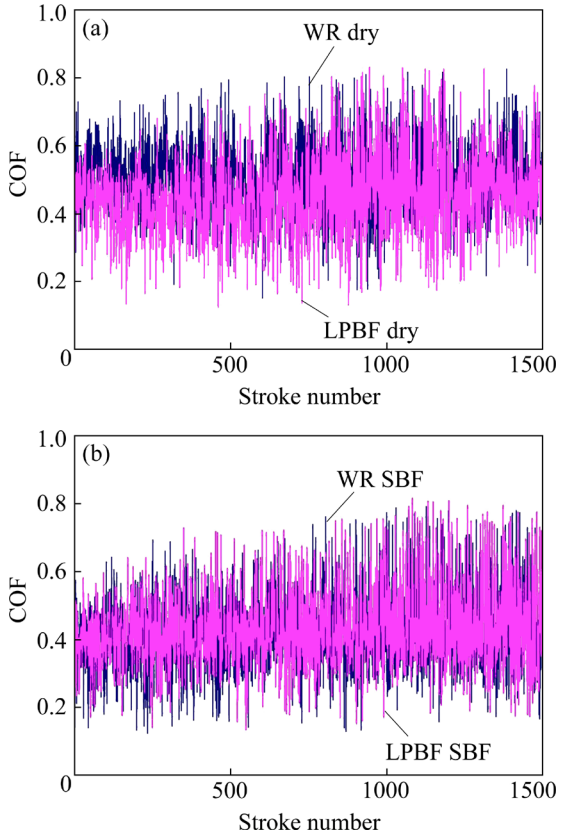

Fig. 7 Variation of COF values during dry sliding (a) and SBF sliding (b) of LPBF and WR Ti-6-4 specimens

Figure 8 presents the wear tracks and the respective depth/width ratios of the LPBF (Figs. 8(a, c)) and WR (Figs. 8(b, d)) alloys under dry (Figs. 8(a, b)) and wet (Figs. 8(c, d)) sliding. As seen in Fig. 8(a), the dry sliding of WR Ti-6-4 against the alumina ball has led to the formation of a wear track of ~610 μm in width and ~13.5 μm in maximum depth, resulting in an average volume loss of 556×10^{-12} m^3 (Fig. 9). The wear track of the LPBF alloy has approximately the same shape, though a lower width (~550 μm) and a lower depth (~11.5 μm) (Fig. 8(b)). This corresponds to a volume loss of 476×10^{-12} m^3, which is reduced by 14.3% relatively to the WR alloy. A distinctive feature of both tracks is the absence of lateral piles

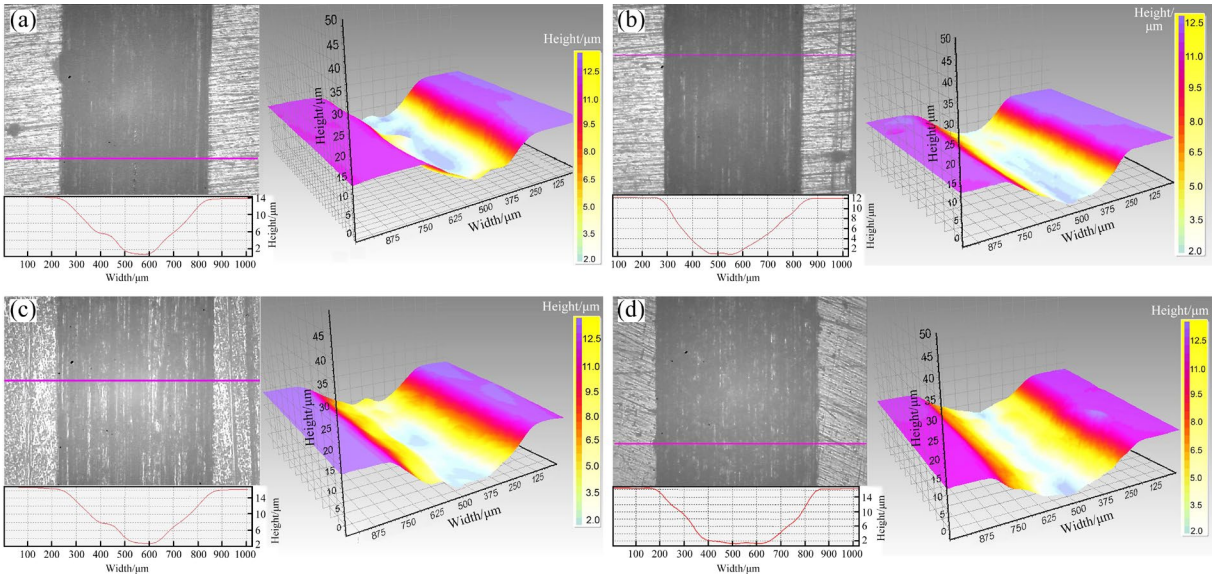

Fig. 8 Wear tracks of LPBF (a, c) and WR (b, d) Ti-6-4: (a, b) Dry sliding; (c, d) SBF sliding

Table 3 Statistical results of COF data of LPBF and WR Ti-6-4

Alloy	COF under dry sliding			COF under SBF sliding		
	Maximum scatter	Average value	2σ interval	Maximum scatter	Average value	2σ interval
WR	0.15−0.83	0.50	0.28−0.72	0.13−0.79	0.43	0.19−0.64
LPBF	0.13−0.83	0.45	0.23−0.67	0.14−0.81	0.41	0.20−0.66

of metal extruded from the track, indicating a low back-side plastic flow of the metal under sliding of the counter-body.

Under wet sliding, both alloys performed similarly, resulting in tracks of similar widths (~650 μm) and maximum depths (~15.5 μm) (Figs. 8(c) and (d)). Accordingly, the WR and LPBF alloys exhibited similar volume losses, with a slight advantage for the WR specimens (596×10^{-12} m^3 against 621×10^{-12} m^3 for LPBF), which is though within statistical error (Fig. 9).

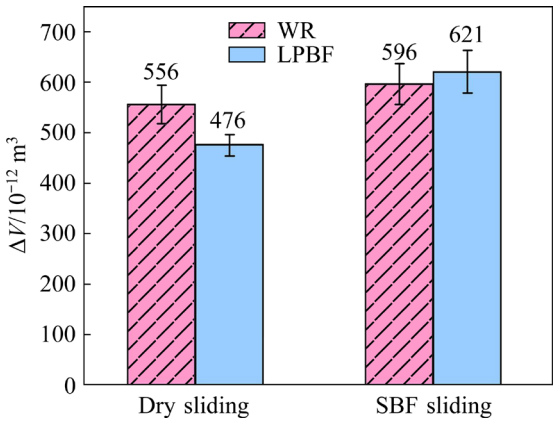

Fig. 9 Mean values of volume loss (ΔV) after dry sliding and SBF sliding

Thus, under dry sliding, LPBF Ti-6-4 outperformed WR Ti-6-4 as regards the tribological (sliding) properties. SBF sliding resulted in levelling-off of the wear resistances of the alloys while their volume losses increased relatively to the dry sliding conditions.

4 Discussion

The differences observed in the corrosion, micromechanical and wear performance of LPBF and WR Ti-6-4 are directly linked with the differences in their microstructure features, which, in turn, are attributed to the fabrication process.

4.1 Micromechanical properties

As follows from Table 1, the LPBF alloy had a significant advantage in the indentation hardness (i.e. the resistance to irreversible and reversible deformation) as compared to the WR alloy. Also, Fig. 4 manifests the superiority of LPBF Ti-6-4 as regards the yield strength σ_y and the ability of the alloy to resist permanent deformation (elastic recovery index, ERI). The main reasons are the fine grain size and the fine-needle α'-martensitic structure

of the LBPF alloy enhancing its strain resistance.

The contribution of the grain size ($\Delta\sigma_{grain}$) to the yield strength σ_y of the alloys was determined by the Hall−Petch relationship:

$$\Delta\sigma_{grain}=k_yD^{-1/2} \quad (6)$$

where k_y is the Hall−Petch coefficient that is a constant specific to the material, and D is the average grain diameter. The k_y value was taken as ~230 MPa·μm$^{1/2}$, a value adopted from CHONG et al [61], who systematically investigated the Hall−Petch relationships in fully equiaxed and bimodal Ti−6Al−4V alloy. A similar value had previously been determined by SEMIATIN and BIELER [62] for a hot-rolled Ti-6-4 alloy strained at a low rate of 0.1 s^{-1} and 900 °C. Taking into account the elongated shape of the grains in the WR alloy (Fig. 2(d)), the grain size was taken as the grain shape aspect ratio (namely, the ratio of the length of a grain to its width). The calculations show that $\Delta\sigma_{grain}$(LPBF Ti-6-4)=63.8 MPa and $\Delta\sigma_{grain}$(WR Ti-6-4)=14.3 MPa; thus, the contribution of the fine grain size to the LPBF alloy's strength is only 49.5 MPa higher than the contribution of the coarse grain size to the WR alloy's strength. This means that the superior strength of the LPBF alloy has mostly been determined by other structural factors, presumably connected with the higher lattice distortion caused by the shear $\beta\rightarrow\alpha'$ transformation (as follows from the broadened α-peaks in the XRD pattern of LPBF Ti-6-4 in Fig. 1).

Table 1 reveals a lower scatter of experimental values for nanoindentation modulus and indentation hardness in the LPBF specimens compared to the WR specimens. This trend can be justified by the more uniform structure of the LPBF alloy, as illustrated in Fig. 10, benefitting a higher homogeneity in property distribution within the sample. In contrast, the WR alloy exhibits more structural heterogeneities (grain size irregularity, grain texture, different compositions and structures along grain boundaries etc.), which have caused a greater scatter of the experimental data.

4.2 Corrosion behavior

Under corrosion testing in SBF at 37 °C, both WR and LPBF alloys displayed very low corrosion rates and true passivity. Moreover, neither alloy underwent localized corrosion. Nevertheless, LPBF

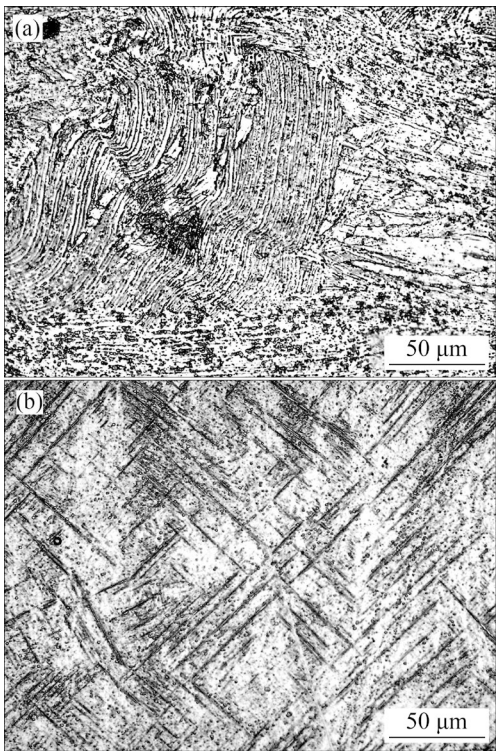

Fig. 10 Comparison of structural homogeneity of WR (a) and LPBF (b) specimens by OM

Ti-6-4 presented higher corrosion rates and higher passivity current densities, attributed to its martensitic structure. Furthermore, as mentioned in Section 3.3, a small number of LPBF specimens presented metastable pitting which, however, was not stabilized. As aforementioned, martensite is a non-equilibrium strained phase of high energy state [25,52] that may induce increased corrosion rates. The high density of defects, such as dislocations and twins [15], may cause the formation of less stable passive films, which are responsible for the increased passivity current densities. Moreover, the supersaturation of α'-phase with V, may deteriorate the barrier properties of the Ti-oxide surface film, since the V-oxides are less stable than Ti-oxides, according to the respective Ellingham diagram [63] and in compatibility with METIKOŠ-HUKOVIĆ et al [64]. Sub-micron porosity does not appear to have caused any significant degradation at least for the specific material (of a highly passivating ability) and conditions.

The dominant microstructure of martensite has also been considered the main reason for the metastable pitting in LPBF Ti-6-4, observed in Fig. 5(d) in Ref. [65]. CUI et al [65,66] interpreted metastable pitting on LPBF Ti-6-4 in Hank's and

NaCl solutions based on the point defect model. In summary, they claimed that titanium atoms replace cation vacancies in the passive film, generating Ti ions that gradually oxidize, creating oxygen vacancies. Aggressive ions like Cl^- are selectively adsorbed on these vacancies, depleting them and creating a local surplus of positive charge. This surplus causes the formation of pairs of cation and oxygen vacancies within the film. Cation vacancies then migrate to the metal/film interface and react with cations. Incomplete consumption of these vacancies can lead to void formation, causing local detachment of the film. Substrate repassivation may induce metastable pitting, which is observed in Fig. 5(d), while failure to repassivate ensues stable pitting. The passive film on martensite has a higher flux of oxygen vacancies, resulting in the adsorption of more aggressive ions compared to the passive film on an α+β dual-phase structure [65].

Regarding the corrosion behavior of WR Ti-6-4, the coexistence of α+β phases in the alloy is considered to form galvanic cells at the α+β boundaries owing to different chemical compositions of the passive films [67−69]. Nevertheless, in the present case, the uniform and very fine distribution of β-phase within the α-matrix (Figs. 2(e−h)) suggests a uniform passive film. Regarding the effect of the grain size on the corrosion resistance, the comparatively fine grain size of the LPBF alloy is expected to benefit its corrosion resistance, since the increased density of the grain boundaries could induce increased nucleation sites for passive film formation [70]. It seems that the negative effect of martensite has surpassed the positive effect of the reduced grain size, leading to a slightly inferior corrosion resistance for LPBF Ti-6-4 compared to its WR counterpart.

4.3 Sliding wear (dry and corrosive) behavior

As shown in Section 3.4, during dry sliding, the LPBF Ti-6-4 exhibited better tribological properties compared to the WR alloy. This can be reasonably explained by the difference in their indentation hardness, which determines the interaction of the rubbing surfaces. The comparatively high wear resistance of the LPBF alloy is associated with its higher hardness, and, consequently, smaller grain size and the predominance of a fine acicular martensitic structure. In the finer grained LPBF alloy, the abundance of grain boundaries per unit area or volume provided numerous barriers to dislocation sliding, thereby impeding plastic deformation [71]. These strengthening factors have lessened the plastic deformation of the LPBF surface (i.e., the ball penetration depth) and, consequently, inhibited the microcrack occurrence under repeated frictional deformation, thus hindering the wear debris formation and delamination [72]. It is well-known that microcracks either on the oxide layer or on the plain wear surface owing to plastic deformation, may eventually lead to material decohesion/ detachment [73]. However, the advantage of the LPBF alloy as regards COF under dry sliding is small, indicating the similarity in the friction forces of the Al_2O_3−LPBF and Al_2O_3−WR counterbodies. The reason for such behavior is that the surface of the softer alloy (WR) is more easily deformed during rubbing, which reduces the formation of a lubricating oxide film.

Under SBF-sliding, the average COF values and the scatter of the COF's variation are somewhat reduced relatively to dry sliding due to the liquid lubrication in the contact zone (Table 3). Lubrication might be facilitated by easy liquid adsorption onto the TiO_2-based oxide film, which usually forms on Ti-based alloys under friction in an oxygen-containing atmosphere [74]. According to KUŹMICZ-MIROSŁAW et al [75], TiO_2 exhibits a remarkable wettability with water and aqueous solutions under UV-irradiation in daylight. However, the decrease in COF is not accompanied by a decrease in volume loss ΔV. Instead, ΔV increased comparatively to dry sliding, reaching about the same level (approximately 600×10^{-12} m^3 in Fig. 9) for both alloys despite their different hardnesses.

The reason for such a response might lie in the corrosion behavior of the alloys where the LPBF alloy showed 2.6 times greater corrosion rate and 1.5 times greater passivity current density in comparison with the WR counterpart (see Table 2). It can be presumed that SBF sliding is accompanied by a tribocorrosion synergism [76], which is a typical phenomenon for wear mechanisms associated with different aggressive media (hydro-abrasion [77], cavitation [78], high-temperature erosion [79], etc.). The tribocorrosion synergism is a serious problem especially for passive metals (including Ti and its alloys), the corrosion

resistance of which mostly depends on the protecting effect of a thin oxide film. When the film is damaged or removed by friction, corrosion is significantly intensified, thus accelerating surface degradation [80]. According to the ASTM G119-04 [81], the total wear rate (T) in a corrosive-active medium is described as

$$T=W_o+C_o+S \tag{7}$$

where W_o is the mechanical wear rate, C_o is the corrosion rate, and S is the tribocorrosion synergy (which is the volume or mass loss rate caused by the interaction of mechanical and corrosion processes).

Synergy S is the sum of the wear-accelerated corrosion (ΔC_w) and corrosion-accelerated wear (ΔW_c) given as [81]

$$\Delta C_w=C_w-C_o \tag{8}$$

$$\Delta W_c=T-(W_o+C_o+\Delta C_w) \tag{9}$$

where C_w is the corrosion rate under wear.

As follows from the dry sliding testing, the LPBF alloy undergoes lower mechanical wear (W_o) mainly due to its higher strength properties. However, the LPBF exhibits a higher corrosion rate (C_o) (Table 2) caused by the strained martensite structure and the stresses remaining after 3D printing. It can thus be presumed that it is the corrosion-wear synergy that is responsible for the lower than expected wear performance of LPBF Ti-6-4 under SBF sliding. This presumption is compatible to the results obtained by YAZDI et al [82], who found that the presence of corrosion caused an increase in the wear rates by 28%−245% under different normal loads in phosphate buffered saline (PBS) solution. Moreover, XU et al [83] noted that corrosion accelerates the wear loss of Ti−16Mo alloy in PBS solution.

As the corroded surface is easily worn under rubbing, the corrosion-accelerated wear (ΔW_c) of the LPBF alloy should significantly contribute to its total wear rate T. The WR alloy presents lower corrosion rate compared to the LPBF alloy owing to its stabilized $\alpha+\beta$ structure with lower residual stresses. However, the WR alloy presents higher mechanical wear rate due to intenser plastic deformation of the surface, which should enhance its wear-accelerated corrosion (ΔC_w). Hence, under SBF-sliding, the total wear rate of the Ti-6-4 alloy was controlled by various factors, some of which (lubrication) might hinder the surface degradation while others (the wear-corrosion synergism) might accelerate it. In the present research, the superposition of these factors resulted in an increase in the volume loss, relatively to dry sliding, and in levelling-off of the wear resistances of the LPBF and WR alloys.

As follows from Eqs. (8) and (9), C_w is a key factor in the tribocorrosion synergy manifestation. Its value can be calculated by the Faraday law [80] presented in the form:

$$C_w=\frac{J_{corr}^{slid}E_W}{F\rho}A \tag{10}$$

where J_{corr}^{slid} is the corrosion current density measured during sliding; F is the Faraday's constant (26.81 A·h/mol); A is the wear track's surface area, ρ is the density of the alloy; E_W is the equivalent mass of the alloy, which is determined as

$$E_W=1\Big/\left[\sum\frac{n_i\cdot f_i}{M_i}\right] \tag{11}$$

where n_i, f_i and M_i are the valence, mass fraction and relative molar mass of the ith alloy element, respectively.

FEYZI et al [84] studied the tribocorrosion of WR Ti-6-4 under conditions close to those of the present research, i.e. sliding against a ZrO_2 ball in PBS under the load of 6 N. They found that the rubbing of the surface increased the anodic current by one order of magnitude (from about 1×10^{-6} A to 5.2×10^{-5} A). In order to roughly calculate C_w by Eq. (10), it was assumed that the same order of magnitude increase in corrosion current could have occurred in the present case.

Based on Table 2, the following values were adopted for the calculation: $J_{corr}^{slid}=5.3\times10^{-4}$ mA/cm^2 (LPBF Ti-6-4), $J_{corr}^{slid}=2.0\times10^{-4}$ mA/cm^2 (WR Ti-6-4), E_W=11.76 g/mol, alloy density ρ=4.51 g/cm^3, and $A=4.6\times10^5$ μm^2 (roughly derived from the images in Fig. 8). Eventually, the C_w values were calculated as 2.37×10^{-16} and 0.895×10^{-6} m^3/h for the LPBF and WR alloys, respectively. Then, the $C_{w,LPBF}/C_{w,WR}$ ratio was 2.7. At the same time, the increase in the volume loss ΔV under SBF-sliding comparatively to dry sliding was 145×10^{-12} m^3 for the LPBF alloy and 40×10^{-12} m^3 for the WR alloy, giving a $\Delta V_{LPBF}/\Delta V_{WR}$ ratio of 3.6. These two values (2.7 and 3.6) are also close, implying that LPBF Ti-6-4 underwent a more significant increase in

volume loss compared to its WR counterpart, which was governed by the wear-accelerated corrosion. For the WR alloy, the wear-accelerated corrosion contributed to a less extent, which led to the levelling-off of the wear behaviors of the two alloys.

The presented results demonstrate that the Ti-6-4 alloy, manufactured by the additive LPBF technology, can certainly be considered a promising alternative to the conventionally fabricated alloy in terms of a combination of micromechanical and electrochemical properties, which characterize its suitability for biomedical use, including joint implant applications. The tribocorrosion response of LPBF Ti-6Al-4V can be improved by additional heat treatment (such as low-temperature annealing) to release the residual stresses and stabilize the martensitic structure. Therefore, this issue requires further research.

5 Conclusions

(1) The microstructure of WR Ti-6-4 mainly consisted of very fine rods of V-rich β (bcc) phase uniformly dispersed within α (hcp) matrix, in a lamellar pattern. Lamellae with the same orientation formed coarse grains, with their boundaries defined by primary α phase. The microstructure of LPBF Ti-6-4 was that of fine-grained martensite featuring fish scale-like and radial flow-like patterns.

(2) Both alloys showed very low corrosion rates (order of 10^{-5} mA/cm^2 or 10^{-4} mm/a) and true passivity current density (order of 10^{-4} mA/cm^2) in the SBF at 37 °C. Neither alloy underwent localized corrosion. Nevertheless, the LPBF alloy presented greater corrosion rates and passivity current densities attributed to its martensitic structure.

(3) LPBF Ti-6-4 featured slightly higher nanoindentation modulus (by ~3%), nanohardness and yield strength (by ~32%), as compared with WR Ti-6-4. On the other hand, the WR alloy showed higher indentation ductility as follows from the higher plasticity index (by ~8%).

(4) The LPBF alloy exhibited better tribological behavior under dry sliding conditions in terms of ~14% lower volume loss and ~5% lower friction coefficient. Under wet sliding in the SBF solution, the volume losses of both the LPBF and WR alloys increased while their wear resistances were levelled-off. Under SBF sliding, the advantage of the LPBF alloy was diminished due to more intensive wear-accelerated corrosion induced by the unstable, stressed martensitic structure.

(5) Overall, the results demonstrate the suitability of LPBF Ti-6-4 for biomedical applications.

CRediT authorship contribution statement

A. G. LEKATOU: Conceptualization, Methodology, Writing − Original draft, Writing − Review & editing; **B. V. EFREMENKO:** Investigation, Writing − Original draft, Writing − Review & editing; **V. HAOUI:** Investigation, Formal analysis; **V. G. EFREMENKO:** Conceptualization, Methodology, Writing − Original draft, Writing − Review & editing, Funding acquisition, Supervision; **S. EMMANOUILIDOU:** Investigation, Data curation; **V. I. ZURNADZHY:** Investigation, Validation; **I. PETRYSHYNETS:** Methodology, Recourses, Funding acquisition; **Yu. G. CHABAK:** Investigation, Project administration; **I. I. SILI:** Validation, Formal analysis.

Declaration of competing interest

The authors declare that they have no known competing financial interests or personal relationships that could have appeared to influence the work reported in this paper.

Acknowledgments

This research was supported by the Ministry of Education and Science of Ukraine (No. 0123U101834). V. G. EFREMENKO, V. I. ZURNADZHY and Yu. G. CHABAK appreciate the support in the framework of the "EU Next generation EU through the Recovery and Resilience Plan for Slovakia" (Nos. 09I03-03-V01-00061 and 09I03-03-V01-00099).

References

[1] ELIAZ N. Corrosion of metallic biomaterials: A review [J]. Materials, 2019, 12: E407.

[2] VASYLYEV M A, MORDYUK B N, BEVZ V P, VOLOSHKO S M, MORDIUK O B. Ultrasonically nanostructured electric-spark deposited Ti surface layer on Ti6Al4V alloy: Enhanced hardness and corrosion resistance [J]. International Journal of Surface Science and Engineering, 2020, 14: 1−15.

[3] LEKATOU A. Engineering alloys [M]. Athens: Papasotiriou Publications, 2005. (in Greek)

[4] MOLINARI A, STRAFFELINI G, B TESI B, BACCI T. Dry sliding wear mechanisms of the Ti6Al4V alloy [J]. Wear, 1997, 208: 105−112.

[5] ZHANG Ming-yuan, ZHAO Xu, MA Ying-juan, ZHANG

Xian-zheng, ZHU Cun-kuan. Investigation on improving the fretting wear properties of Ti6Al4V alloy via micro-shot peening to produce surface asperities and surface hardening layer [J]. Journal of Materials Engineering and Performance, 2025, 34: 2835−2849.

[6] WEI Gui-jiang, TAN Mei-ying, ATTARILAR S, LI Jie, UGLOV V V, WANG Bing-hao, LIU Jia, LU Lu, WANG Li-qiang. An overview of surface modification, A way toward fabrication of nascent biomedical Ti−6Al−4V alloys [J]. Journal of Materials Research and Technology, 2023, 24: 5896−5921.

[7] EFREMENKO V G, LEKATOU A G, CHABAK Yu G, EFREMENKO B V, PETRYSHYNETS I, ZURNADZHY V I, EMMANOUILIDOU S, VOJTKO M. Micromechanical, corrosion and wet sliding wear behaviours of Co−28Cr−6Mo alloy: Wrought vs. LPBF [J]. Materials Today Communications, 2023, 35: 105936.

[8] AZAR A S, LEKATOU A, SUNDING M E, GRAFF J S, TZIMA N, DIPLAS S. Corrosion performance and degradation mechanism of a bi-metallic aluminum structure processed by wire-arc additive manufacturing [J]. NPJ Materials Degradation, 2021, 5: 26.

[9] KAROLEWSKA K, LIGAJ B. Comparison analysis of titanium alloy Ti6Al4V produced by metallurgical and 3D printing method [J]. AIP Conference Proceedings, 2019, 2077: 020025.

[10] ZHANG Lai-chang, CHEN Liang-yu, ZHOU Sheng-feng, LUO Zhen. Powder bed fusion manufacturing of beta-type titanium alloys for biomedical implant applications: A review [J]. Journal of Alloys and Compounds, 2023, 936: 168099.

[11] LIU Shun-yu, SHIN Yung. Additive manufacturing of Ti6Al4V alloy: A review [J]. Materials & Design, 2019, 164: 107552.

[12] NGUYEN H D, PRAMANIK A, BASAK A K, DONG Y, PRAKASH C, DEBNATH S, SHANKAR S, JAWAHIR I S, DIXIT S, BUDDHI D. A critical review on additive manufacturing of Ti−6Al−4V alloy: Microstructure and mechanical properties [J]. Journal of Materials Research and Technology, 2022, 18: 4641−4661.

[13] NEIKTER M, ÅKERFELDT P, PEDERSON R, ANTTI M L, SANDELL V. Microstructural characterization and comparison of Ti−6Al−4V manufactured with different additive manufacturing processes [J]. Materials Characterization, 2018, 143: 68−75.

[14] XU Ming-fang, CHEN Yu-hua, ZHANG Ti-ming, XIE Ji-lin, WANG Shan-lin, YIN Li-meng, HE Peng. Microstructure evolution and mechanical properties of wrought/wire arc additive manufactured Ti−6Al−4V joints by electron beam welding [J]. Materials Characterization, 2022, 190: 112090.

[15] HUANG Qian-li, HU Ning-min, YANG Xing, ZHANG Ran-ran, FENG Qing-ling. Microstructure and inclusion of Ti−6Al−4V fabricated by selective laser melting [J]. Frontiers of Materials Science, 2016, 10: 428−431.

[16] CHEN Xin-yue, XIE Xin-liang, WU Hao, JI Xia, SHEN Hao-peng, XUE Mu-han, WU He, CHAO Qi, FAN Guo-hua, LIU Qing. In-situ control of residual stress and its distribution in a titanium alloy additively manufactured by laser powder bed fusion [J]. Materials Characterization, 2023, 201: 112953.

[17] AN Na-ying, SHUAI San-san, CHEN Chao-yue, LEI Li-ming, WANG Jiang, REN Zhong-ming. Quantitative study of geometric characteristics and formation mechanism of porosity defects in selective laser melted Ti6Al4V alloy by micro-computed tomography [J]. Transactions of Nonferrous Metals Society of China, 2023, 33: 2986−3002.

[18] ZHANG Qi, LIANG Zheng-long, CAO Miao, LIU Zi-fan, ZHANG An-feng, LU Bing-heng. Microstructure and mechanical properties of Ti6Al4V alloy prepared by selective laser melting combined with precision forging [J]. Transactions of Nonferrous Metals Society of China, 2017, 27: 1036−1042.

[19] BARRIOBERO-VILA P, GUSSONE J, HAUBRICH J, SANDLÖBES S, DA SILVA J C, CLOETENS P, SCHELL N, REQUENA G. Inducing stable α+β microstructures during selective laser melting of Ti−6Al−4V using intensified intrinsic heat treatments [J]. Materials, 2017, 10: E268.

[20] QIN Peng, CHEN Liang-yu, LIU Yu-jing, LIANG Shun-xing, SUN Hon-qi, ZHANG Lai-chang. Corrosion and passivation behavior of laser powder bed fusion produced Ti−6Al−4V under various prior plastic deformation strains [J]. Corrosion Science, 2024, 230: 111919.

[21] QIN P, CHEN L Y, LIU Y J, JIA Z, LIANG S X, ZHAO C H, SUN H, ZHANG L C. Corrosion and passivation behavior of laser powder bed fusion produced Ti−6Al−4V in static/dynamic NaCl solutions with different concentrations [J]. Corrosion Science, 2021, 191: 109728.

[22] CHEN Liang-yu, ZHANG Hong-yue, ZHENG Chuan-bo, YANG Hong-yu, QIN Peng, ZHAO Cui-hua, LU Sheng, LIANG Shun-xing, CHAI Lin-jiang, ZHANG Lai-chang. Corrosion behavior and characteristics of passive films of laser powder bed fusion produced Ti−6Al−4V in dynamic Hank's solution [J]. Materials & Design, 2021, 208: 109907.

[23] BOWER K, MURRAY S, REINHART A, NIETO A. Corrosion resistance of selective laser melted Ti−6Al−4V alloy in salt fog environment [J]. Results in Materials, 2020, 8: 100122.

[24] WANG Xin, QIN Peng, CHEN Liang-yu, SUN Hong-qi, ZHANG Lai-chang. Corrosion behavior and mechanisms of the heat-treated Ti5Cu produced by laser powder bed fusion [J]. Corrosion Science, 2023, 221: 111336.

[25] DAI Nian-wei, ZHANG Lai-chang, ZHANG Jun-xi, ZHANG Xin, NI Qing-zhao, CHEN Yang, WU Mao-liang, YANG Chao. Distinction in corrosion resistance of selective laser melted Ti−6Al−4V alloy on different planes [J]. Corrosion Science, 2016, 111: 703−710.

[26] HUANG Xin, LIU Heng, WANG Ze-ning, QIAO Li-jie, SU Yan-jing, YAN Yu. Effect of surface oxidation on wear and tribocorrosion behavior of forged and selective laser melting-based TC4 alloys [J]. Tribology International, 2022, 174: 107780.

[27] SHARMA A, OH M C, KIM J T, SRIVASTAVA A K, AHN B. Investigation of electrochemical corrosion behavior of additive manufactured Ti−6Al−4V alloy for medical implants in different electrolytes [J]. Journal of Alloys and Compounds, 2020, 830: 154620.

[28] ETTEFAGH A H, ZENG C Y, GUO S M, RAUSH J. Corrosion behavior of additively manufactured Ti−6Al−4V parts and the effect of post annealing [J]. Additive

Manufacturing, 2019, 28: 252−258.

[29] DAI Nian-wei, ZHANG Lai-chang, CHEN Qi-meng, ZHANG Jun-xi, WU Mao-liang. Corrosion behavior of selective laser melted Ti−6Al−4V alloy in NaCl solution [J]. Journal of the Electrochemical Society, 2017, 164: 428−434.

[30] MORA-SANCHEZ H, RAMOS C, MOHEDANO M, TORRES B, ARRABAL R, MATYKINA E. Flash plasma electrolytic oxidation and electrochemical behaviour in physiological media of additive manufacturing Ti6Al4V alloy [J]. Transactions of Nonferrous Metals Society of China, 2024, 34: 1150−1166.

[31] CECCHEL S, MONTESANO L, CORNACCHIA G. Wear and corrosion characterization of a Ti−6Al−4V component for automotive applications: Forging versus selective laser melting technologies [J]. Advanced Engineering Materials, 2022, 24: 2200082.

[32] JU Jiang, LI Jing-jing, JIANG Min, LI Meng-ya, YANG Li-xiang, WANG Kai-ming, YANG Chao, KANG Mao-dong, WANG Jun. Microstructure and electrochemical corrosion behavior of selective laser melted Ti−6Al−4V alloy in simulated artificial saliva [J]. Transactions of Nonferrous Metals Society of China, 2021, 31: 167−177.

[33] VILHENA L M, SHUMAYAL A, RAMALHO A, MARTINS FERREIRA J A. Tribocorrosion behaviour of Ti6Al4V produced by selective laser melting for dental implants [J]. Lubricants, 2020, 8: 22.

[34] LIU Zheng, ZHANG Lian-min, REN De-chun, MA Ai-li, JI Hai-bin, ZHENG Yu-gui. Corrosion behavior of Ti−6Al−4V alloy fabricated by selective laser melting in simulated spent fuel reprocessing environment [J]. Transactions of Nonferrous Metals Society of China, 2024, 34: 2167−2180.

[35] LI Hua, CHEN Zhan Wen, RAMEZANI M. Effect of temperature on sliding wear behavior of Ti−6Al−4V alloy processed by Powder Bed Fusion additive manufacturing techniques [J]. Journal of Materials Engineering and Performance, 2022, 31: 8940−8954.

[36] BARTOLOMEU F, BUCIUMEANU M, PINTO E, ALVES N, SILVA F S, CARVALHO O, MIRANDA G. Wear behavior of Ti6Al4V biomedical alloys processed by selective laser melting, hot pressing and conventional casting [J]. Transactions of Nonferrous Metals Society of China, 2017, 27: 829−838.

[37] ZHU Y, CHEN X, ZOU J, YANG H. Sliding wear of selective laser melting processed Ti6Al4V under boundary lubrication conditions [J]. Wear, 2016, 368/369: 485−495.

[38] ZHANG Wei-wen, QIN Pei-ting, WANG Zhi, YANG Chao, KOLLO L, GRZESIAK D, PRASHANTH K G. Superior wear resistance in EBM-processed TC4 alloy compared with SLM and forged samples [J]. Materials (Basel), 2019, 12: E782.

[39] KANG Nan, EL MANSORI M, FENG En-hao, ZHAO Chun-ling, ZHAO Yu, LIN Xin. Sliding wear and induced-microstructure of Ti−6Al−4V alloys: Effect of additive laser technology [J]. Tribology International, 2022, 173: 107633.

[40] TOPTAN F, ALVES A C, CARVALHO Ó, BARTOLOMEU F, PINTO A M P, SILVA F, MIRANDA G. Corrosion and tribocorrosion behaviour of Ti6Al4V produced by selective laser melting and hot pressing in comparison with the commercial alloy [J]. Journal of Materials Processing Technology, 2019, 266: 239−245.

[41] CHIU T M, MAHMOUDI M, DAI W, ELWANY A, LIANG H, CASTANEDA H. Corrosion assessment of Ti−6Al−4V fabricated using laser powder-bed fusion additive manufacturing [J]. Electrochimica Acta, 2018, 279: 143−151.

[42] CHABAK Y, EFREMENKO B, PETRYSHYNETS I, EFREMENKO V, LEKATOU A G, ZURNADZHY V, BOGOMOL I, FEDUN V, KOVAL' K, PASTUKHOVA T. Structural and tribological assessment of biomedical 316 stainless steel subjected to pulsed-plasma surface modification: comparison of LPBF 3D printing and conventional fabrication [J]. Materials (Basel), 2021, 14: 7671.

[43] BELLINI D, CENCETTI C, MERANER J, STOPPOLONI D, D'ABUSCO A S, MATRICARDI P. An in-situ gelling system for bone regeneration of osteochondral defects [J]. European Polymer Journal, 2015, 72: 642−650.

[44] SFIKAS A K, LEKATOU A G. Electrochemical behavior of Al−Al_9Co_2 alloys in sulfuric acid [J]. Corrosion and Materials Degradation, 2020, 1: 249−272.

[45] LEKATOU A G, TSOULI S. Cyclic polarization of corrugated austenitic stainless steel rebars in acid rain: Effect of fly ash, pH and steel type [J]. Corrosion and Materials Degradation, 2022, 3: 75−100.

[46] ASTM G102-89(2015)e1. Standard Practice for Calculation of Corrosion Rates and Related Information from Electrochemical Measurement [S]. ASTM International, 2015.

[47] LEKATOU A G, SIOULAS D, GRIMANELIS D. Corrosion and wear of coatings fabricated by HVOF-spraying of nanostructured and conventional WC−10Co−4Cr powders on Al7075-T6 [J]. International Journal of Refractory Metals and Hard Materials, 2023, 112: 106164.

[48] DIMITRIADIS K, LEKATOU A G, SFIKAS A K, ROUMPI M, TSOULI S, GALIATSATOS A, AGATHOPOULOS S. Influence of heat-treatment cycles on the microstructure, mechanical properties, and corrosion resistance of Co−Cr dental alloys fabricated by selective laser melting [J]. Journal of Materials Engineering and Performance, 2021, 30: 5252−5265.

[49] EFREMENKO V G, CHABAK Y G, FEDUN V I, SHIMIZU K, PASTUKHOVA T V, PETRYSHYNETS I, ZUSIN A M, KUDINOVA E V, EFREMENKO B V. Formation mechanism, microstructural features and dry-sliding behaviour of "Bronze/WC carbide" composite synthesised by atmospheric pulsed-plasma deposition [J]. Vacuum, 2021, 185: 110031.

[50] BAI Yun, GAI Xin, LI Shu-jun, ZHANG Lai-chang, LIU Yu-jing, HAO Yu-lin, ZHANG Xing, YANG Rui, GAO Yong-bo. Improved corrosion behaviour of electron beam melted Ti−6Al−4V alloy in phosphate buffered saline [J]. Corrosion Science, 2017, 123: 289−296.

[51] APPOLAIRE B, HÉRICHER L, AEBY-GAUTIER E. Modelling of phase transformation kinetics in Ti alloys—Isothermal treatments [J]. Acta Materialia, 2005, 53: 3001−3011.

[52] DAI Nian-wei, ZHANG Lai-chang, ZHANG Jun-xi, CHEN Qi-meng, WU Mao-liang. Corrosion behavior of selective

laser melted Ti−6Al−4V alloy in NaCl solution [J]. Corrosion Science, 2016, 102: 484−489.

[53] SHI Rong-pei, ZHENG Yu-feng, BANERJEE R, FRASER H L, WANG Yun-zhi. ω-Assisted α nucleation in a metastable β titanium alloy [J]. Scripta Materialia, 2019, 171: 62−66.

[54] AHMED T, RACK H J. Phase transformations during cooling in α+β titanium alloys [J]. Materials Science and Engineering: A, 1998, 243: 206−211.

[55] REED R. The superalloys: Fundamentals and applications [M]. Cambridge: Cambridge Universities Press, 1998.

[56] TAO Ping, GONG Jian-ming, WANG Yan-fei, JIANG Yong, LI Yang, CEN Wei-wei. Characterization on stress−strain behavior of ferrite and austenite in a 2205 duplex stainless steel based on nanoindentation and finite element method [J]. Results in Physics, 2018, 11: 1377−1384.

[57] RODRÍGUEZ R, GUTIERREZ I. Correlation between nanoindentation and tensile properties: Influence of the indentation size effect [J]. Materials Science and Engineering: A, 2003, 361: 377−384.

[58] OKORO A M, LEPHUTHING S S, RASIWELA L, OLUBAMBI P A. Nondestructive measurement of the mechanical properties of graphene nanoplatelets reinforced nickel aluminium bronze composites [J]. Heliyon, 2021, 7: e07978.

[59] LEKATOU A G, EMMANOUILIDOU S, DIMITRIADIS K, BAIKOUSI M, KARAKASSIDES M A, AGATHOPOULOS S. Simulating porcelain firing effect on the structure, corrosion and mechanical properties of Co−Cr−Mo dental alloy fabricated by soft milling [J]. Odontology, 2024, 112: 372−389.

[60] QU J, BLAU P J, WATKINS T R, CAVIN O B, KULKARNI N S. Friction and wear of titanium alloys sliding against metal, polymer, and ceramic counterfaces [J]. Wear, 2005, 258: 1348−1356.

[61] CHONG Yan, DENG Guan-yu, GAO Si, YI Jangho, SHIBATA A, TSUJI N. Yielding nature and Hall−Petch relationships in Ti−6Al−4V alloy with fully equiaxed and bimodal microstructures [J]. Scripta Materialia, 2019, 172: 77−82.

[62] SEMIATIN S L, BIELER T R. The effect of alpha platelet thickness on plastic flow during hot working of Ti−6Al−4V with a transformed microstructure [J]. Acta Materialia, 2001, 49: 3565−3573.

[63] JOHNSON C E, JOHNSON I, KOPASZ J P. Thermodynamic considerations for the use of vanadium alloys with ceramic breeder materials: USA Patent, ANL/CMT/CP-88542 [P]. 1995.

[64] METIKOŠ-HUKOVIĆ M, KWOKAL A, PILJAC J. The influence of niobium and vanadium on passivity of titanium-based implants in physiological solution [J]. Biomaterials, 2003, 24: 3765−3775.

[65] CUI Yu-wei, CHEN Liang-yu, QIN Peng, LI Rui-feng, ZANG Qian-hao, PENG Jin-hua, ZHANG Li-na, LU Sheng, WANG Li-qiang, ZHANG Lai-chang. Metastable pitting corrosion behavior of laser powder bed fusion produced Ti−6Al−4V in Hank's solution [J]. Corrosion Science, 2022, 203: 110333.

[66] CUI Yu-wei, CHEN Liang-yu, CHU Yu-hang, ZHANG Li-na, LI Rui-feng, LU Sheng, WANG Li-qiang, ZHANG Lai-chang. Metastable pitting corrosion behavior and characteristics of passive film of laser powder bed fusion produced Ti−6Al−4V in NaCl solutions with different concentrations [J]. Corrosion Science, 2023, 215: 111017.

[67] QIN Peng, CHEN Yang, LIU Yu-jing, ZHANG Jun-xi, CHEN Liang-yu, LI Yu-hua, ZHANG Xu-hui, CAO Chong-de, SUN Hong-qi, ZHANG Lai-chang. Resemblance in corrosion behavior of selective laser melted and traditional monolithic Ti−24Nb−4Zr−8Sn alloy, ACS Biomaterials Science & Engineering, 2019, 5(2):1141−1149.

[68] ZADEH M K, YEGANEH M, SHOUSHTARI M T, RAMEZANALIZADEH H, SEIDI F. Microstructure, corrosion behavior, and biocompatibility of Ti−6Al−4 V alloy fabricated by LPBF and EBM techniques [J]. Materials Today Communications, 2022, 31: 103502.

[69] YU Jun, QIN Tuo, LIN Xin, WANG Jun-jie, ZHANG Yu-feng, WANG Shi-yao, YANG Jing-yi, HUANG Wei-dong. Electrochemical dissolution and passivation of laser additive manufactured Ti6Al4V controlled by elements segregation and phases distribution [J]. Transactions of Nonferrous Metals Society of China, 2021, 31: 3739−3751.

[70] HUANG Run, HAN Yong. The effect of SMAT-induced grain refinement and dislocations on the corrosion behavior of Ti−25Nb−3Mo−3Zr−2Sn alloy [J]. Materials Science and Engineering: C, 2013, 33: 2353−2359.

[71] LEKATOU A G, SFIKAS A K, KARANTZALIS A E. The influence of the fabrication route on the microstructure and surface degradation properties of Al reinforced by Al_9Co_2 [J]. Materials Chemistry and Physics, 2017, 200: 33−49.

[72] CHABAK Y, EFREMENKO V, ZURNADZHY V, PUCHÝ V, PETRYSHYNETS I, EFREMENKO B, FEDUN V, SHIMIZU K, BOGOMOL I, KULYK V, JAKUBÉCZYOVÁ D. Structural and tribological studies of "(TiC+WC)/ hardened steel" PMMC coating deposited by air pulsed plasma [J]. Metals, 2022, 12: 218.

[73] KARANTZALIS A E, LEKATOU A, TSIRKA K. Solidification observations and sliding wear behavior of vacuum arc melting processed Ni−Al−TiC composites [J]. Materials Characterization, 2012, 69: 97−107.

[74] ASHOK R J, SATISH V K. Evolution of wear debris morphology during dry sliding of Ti−6Al−4V against SS316L under ambient and vacuum conditions [J]. Wear, 2020, 456/457: 203378.

[75] KUŹMICZ-MIROSŁAW E, KUŚMIERZ M, TERPIŁOWSKI K, ŚMIETANA M, BARCZAK M, STANISZEWSKA M. Effect of various surface treatments on wettability and morphological properties of titanium oxide thin films [J]. Materials (Basel), 2022, 15: 4113.

[76] LANDOLT D, MISCHLER S. Tribocorrosion of passive metals and coatings [M]. Boston: Woodhead Publishing, 2011.

[77] TUTAR M, AYDIN H, DURMUS A, BAYRAM A, YIGIT K. The hydro-abrasive erosion wear behavior of duplex-treated surfaces of AISI H13 tool steel [J]. Science China Technological Sciences, 2014, 57: 1040−1051.

[78] SASAKI H, TAKEO F, SOYAMA H. Cavitation erosion resistance of the titanium alloy Ti−6Al−4V manufactured through additive manufacturing with various peening methods [J]. Wear, 2020, 462/463: 203518.

[79] EFREMENKO B V, SHIMIZU K , ESPALLARGAS N, EFREMENKO V G, KUSUMOTO K, CHABAK Y G, BELIK A G, CHIGAREV V V, ZURNADZHY V I. High-temperature solid particle erosion of Cr−Ni−Fe−C arc cladded coatings [J]. Wear, 2020, 460/461: 203439.
[80] MISCHLER S, MUÑOZ A I. Wear of CoCrMo alloys used in metal-on-metal hip joints: A tribocorrosion appraisal [J]. Wear, 2013, 297: 1081−1094.
[81] ASTM G119-04. Standard guide for determining synergism between wear and corrosion [S]. ASTM International, 2004.
[82] YAZDI R, GHASEMI H M, ABEDINI M, WANG C, NEVILLE A, Tribocorrosion behaviour of Ti6Al4V under various normal loads in phosphate buffered saline solution [J]. Transactions of Nonferrous Metals Society of China, 2020, 30: 1300−1314.
[83] XU Wei, YU Ai-hua, LU Xin, TAMADDON M, HAYAT M, WANG Meng-di, ZHANG Jian-liang, QU Xuan-hui, LIU Chao-zong. Synergistic interactions between wear and corrosion of Ti−16Mo orthopedic alloy [J]. Journal of Materials Research and Technology, 2020, 9: 9996−10003.
[84] FEYZI M, FALLAHNEZHAD K, TAYLOR M, HASHEMI R. The tribocorrosion behaviour of Ti−6Al−4V alloy: The role of both normal force and electrochemical potential [J]. Tribology Letters, 2022, 70: 83.

激光粉末床熔融和锻造医用 Ti−6Al−4V 合金的显微组织、电化学、磨损和腐蚀磨损性能

A. G. LEKATOU[1,2], B. V. EFREMENKO[3], V. HAOUI[1], V. G. EFREMENKO[3,4], S. EMMANOUILIDOU[1], V. I. ZURNADZHY[3,4], I. PETRYSHYNETS[4], Yu. G. CHABAK[3,4], I. I. SILI[3]

1. Laboratory of Applied Metallurgy, Department of Materials Science and Engineering, School of Engineering, University of Ioannina, Ioannina 45110, Greece;
2. Institute of Materials Science and Computing, University Research Center of Ioannina (URCI), Ioannina 45110, Greece;
3. Department of Physics, Pryazovskyi State Technical University, Dnipro 49044, Ukraine;
4. Institute of Materials Research of Slovak Academy of Sciences, Kosice 04001, Slovakia

摘　要：为了判断激光粉末床熔融(LPBF)Ti−6Al−4V(Ti-6-4)是否适用于生物医学领域，对比评估了锻造态和 LPBF Ti−6Al−4V 试样。测试包括纳米压痕、在模拟体液(SBF，37 ℃)中的循环极化，以及在干燥和 SBF 环境下的“球−盘”滑动摩擦。结果表明，锻造态 Ti-6-4 合金的显微组织为层状 α+β 相，而 LPBF Ti-6-4 合金的显微组织为细晶 α'马氏体。LPBF 态 Ti-6-4 合金比锻造钛 Ti-6-4 合金的压痕模量高约 3%，硬度高约 32%，而锻造态 Ti-6-4 合金比 LPBF Ti-6-4 合金的塑性高约 8%。两种合金均表现出较低的腐蚀速率(10^{-5} mA/cm^2 数量级)和真钝化特性(10^{-4} mA/cm^2 数量级)。两种合金均未出现局部腐蚀，仅在 LPPF 钛合金中偶尔观察到亚稳态点蚀。由于马氏体组织的影响，LPBF 态 Ti-6-4 合金具有更高的腐蚀速率和钝化电流。在干滑动摩擦条件下，LPBF Ti-6-4 合金比锻造态 Ti-6-4 合金的体积损失低约 14%；而在 SBF 中滑动时，两种合金的体积损失均增加。马氏体在应力作用下更强烈的磨损加速腐蚀，导致 LPBF Ti-6-4 合金的优势减弱，两种合金的耐磨性能接近。总体而言，LPBF Ti-6-4 合金适用于生物医学领域。

关键词：医用 Ti−6Al−4V 合金；激光粉末床熔融；电化学腐蚀；纳米压痕；滑动磨损；磨损−腐蚀协同

(Edited by Wei-ping CHEN)